Chapter 14

Modeling and Design of BAW Resonators and Filters for Integration in a UMTS Transmitter

Matthieu Chatras , Stéphane Bila, Sylvain Giraud, Lise Catherinot, Ji Fan, Dominique Cros, Michel Aubourg, Axel Flament, Antoine Frappé, Bruno Stefanelli, Andreas Kaiser, Andreia Cathelin, Jean Baptiste David, Alexandre Reinhardt, Laurent Leyssenne and Eric Kerhervé

Additional information is available at the end of the chapter

http://dx.doi.org/10.5772/56026

1. Introduction

Bulk-Acoustic Wave (BAW) resonators and filters are highly integrated devices, which represent an effective alternative for narrow-band components (up to 5% fractional bandwidth) up to few GHz [1].

This chapter presents the integration of a BAW filter and of a BAW duplexer in a UMTS transmitter. The first section details one dimensional and three-dimensional techniques for the modeling and the design of BAW resonators. The second section proposes a synthesis approach for dimensioning BAW filters and the third section illustrates the approach with the characterization of several fabricated prototypes. Finally, The UMTS transmitter incorporating a BAW filter and a BAW duplexer is described with a particular emphasis on the performances of these devices.

2. Model and design of bulk acoustic wave resonators

2.1. Modeling of a BAW resonator in 1 dimension

The proposed method compares the impedance of a piezoelectric resonator obtained by both an electrical equivalent model and a piezoelectric model. By this way, it is possible to obtain the values of the electrical model as functions of all geometrical and material characteristics. The two models and their relation are described in the following sections.

2.1.1. Resonator impedance based on electrical (BVD) model

A piezoelectric resonator can be modeled by the lossless BVD (Butterworth Van Dick) model as shown in Figure 1(a)) [2], [3]. C_o is the geometric capacitance of the structure and the L_m C_m series circuit (called the motional arm) represents the mechanical resonance (motional behavior). According to the circuit in Figure 1 (a), two resonances are obtained, and the equivalent impedance Z_{BVD} of this circuit can be easily derived:

$$f_s = \frac{1}{2\pi\sqrt{L_m C_m}} \tag{1}$$

$$f_p = f_s\sqrt{\frac{C_m + C_o}{C_o}} \tag{2}$$

$$Z_{BVD} = \frac{j(\omega L_m + 1/\omega C_m)}{1 - \omega^2 C_o L_m + C_o / C_m} \tag{3}$$

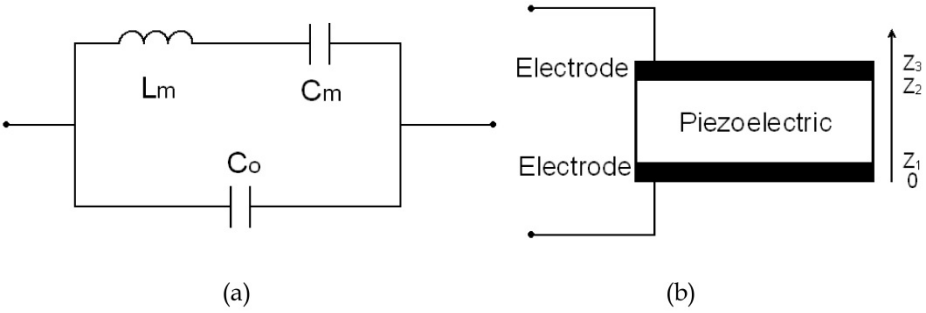

Figure 1. (a) Equivalent circuit of the lossless BVD model. (b) One-dimensional structure piezoelectric resonator.

2.1.2. Resonator impedance based on piezoelectric equations

The description of a piezoelectric resonator, made of a single piezoelectric layer and two thin electrodes as depicted in Figure 1 (b), is considered. Using piezoelectric fundamental equations [4], one can write:

$$T(z) = cS(z) - eE(z) \tag{4}$$

$$D = eS(z) + \varepsilon E(z) \tag{5}$$

$$S(z) = \frac{\partial u(z)}{\partial z} \tag{6}$$

$$-\rho^2 u(z) = \frac{\partial T(z)}{\partial z} \tag{7}$$

In the above equations, T is the mechanical stress tensor, S is the strain tensor, E is the electric field, D is the electrical displacement vector (C/m2), ϱ is the density, u is the mechanical displacement vector, c is the elastic stiffness tensor calculated at constant electric field, e is the piezoelectric tensor (C/m2), and ε is the relative permittivity.

Using the boundaries conditions for T (z) and u(z), we have:

$$T_1(0) = 0 \; ; \quad T_3(z_3) = 0 \tag{8}$$

$$T_1(z_1) = T_2(z_1) \; ; \quad u_1(z_1) = u_2(z_1) \tag{9}$$

$$T_2(z_2) = T_3(z_2) \; ; \quad u_2(z_2) = u_3(z_2) \tag{10}$$

The potential difference u on the piezoelectric layer can be obtained by integrating Ez (the electric field) on the thickness of the considered layer:

$$U = -\int_{z2}^{z1} Ez(z)dz \tag{11}$$

By definition, the current I is the temporal derivation of the charge Q at the surface of the electrodes, which in sinusoidal mode is equivalent to:

$$\mathrm{I} = \mathrm{j}wQ \tag{12}$$

The continuity of the normal component of the electrical displacement vector D at the interface piezoelectric-metal makes it possible to express the charge Q as a function of D and of the surface of the metal electrodes:

$$Q = Dz \; S \tag{13}$$

The expression of the current becomes then:

$$I = \mathrm{j}wS\,Dz \tag{14}$$

Consequently, the impedance of the piezoelectric layer can be obtained in function of the thickness of the used materials and the dimensions of the resonator, as written in equation (15):

$$Z_{eq} = \frac{U}{I} = \frac{[(z_2 - z_1) - \alpha e_2(r_{21} - r_{11}) - \beta e_2(r_{22} - r_{12})] / \varepsilon_2}{j\omega A} \tag{15}$$

Where e_2 is the piezoelectric tensor of the piezoelectric layer, A is the surface (area) of the electrodes, ε_2 is the permittivity of the piezoelectric layer, and r_{11}, r_{12}, r_{21}, r_{22}, α, and β are expressions in function of known constants.

The impedance can be evaluated knowing the material properties and dimensions. This method can also be used for more complex structures, such as SCF (Stacked Crystal Filters), or CRF (Coupled Resonator Filters) resonators or filters, accounting for all the layers.

2.1.3. Equivalence of one dimensional models

Using a least squares method, the two expressions in equations (3) and (15) can be equated. By this way, the values of C_o, C_m and L_m for different resonator areas A and for the thicknesses of each layer can be obtained.

For example, the expression of L_m as a function of the surface A and the thickness t of the top electrode is presented. For fixed values, $[A_1\ A_2\ A_3 \cdots\cdots A_i]$ and $[t_1\ t_2\ t_3 \cdots\cdots\ t_i]$, we obtain corresponding values of L_m. For each same thickness t_i, we can consider that L_m is only varying according to the surface A. As shown in equation (16), we can find a polynomial function in the variable A fitting the values of L_m. The polynomial coefficients (W_i, X_i, Y_i and Z_i) are now independent of the surface A and depend only on the thickness t. In a second time, using the same method, the coefficients can be expressed as a function of variable t.

$$\begin{aligned} L_m &= W_i A^n + X_i A^{n-1} + \cdots\cdots + Y_i A + Z_i \\ &= \left(\sum_{j=1}^{N} a_j t^{j-1}\right) A^n + \left(\sum_{j=1}^{N} b_j t^{j-1}\right) A^{n-1} + \cdots\cdots + \left(\sum_{j=1}^{N} c_j t^{j-1}\right) A + \left(\sum_{j=1}^{N} d_j t^{j-1}\right) \end{aligned} \tag{16}$$

This identification method can also be applied to the other variables, such as the thickness of the loading layer. The three elements of the BVD model (C_o, C_m and L_m) can be determined as functions of the piezoelectric resonator dimensions (thickness of each layer and surface of resonator). According to the expressions of C_o, L_m, and C_m, surfaces and thicknesses can be optimized with an electrical software for designing a BAW resonator or a BAW filter.

2.2. Model in 3 dimensions

Even though Film Bulk Acoustic Resonator simulation with 1D model enables to quickly compute complex frequency response as filters, it becomes too restrictive when spurious modes in lateral dimensions have to be predicted. The 3D Finite Elements Method (FEM) enables to investigate the effect of the electrode shape on the spurious modes that are present in the electrical impedance. In order to reduce or to suppress these modes, solutions have to be investigated.

2.2.1. Finite element model

Piezoelectricity is a phenomenon which couples electrical and mechanical domains. It can be modeled into coupled equations:

$$T_{ij} = c_{ijkl} * S_{kl} - e_{ijk} * E_k \tag{17}$$

$$D_k = e_{kl} * E_l + e_{ijk} * S_{ij} \quad (18)$$

With: T: mechanical stress (Pa), E: electric field (V/m), S: mechanical strain, D: electric displacement(C/m²), c: stiffness tensor (Pa), ε : permittivity tensor (F/m) and e: piezoelectric tensor (C/m²)

Unfortunately, one-dimensional approximation becomes too restrictive when we need to predict spurious modes that may appear with lateral direction mode coupling or with resonators electrical or mechanical cross coupling. Thus a 3D simulation tool is needed to compute the resonator in three dimensions.

In the following sections, examples of 3D FEM computation will be proposed and described highlighting the advantages of 3D simulations.

2.2.2. Mechanical displacement modes

We have analyzed the suspended resonator structure presented in Figure 2. The structure is clamped on lateral sides (no mechanical displacement in space directions), the bottom electrode is grounded and a potential constraint is applied to the top electrode.

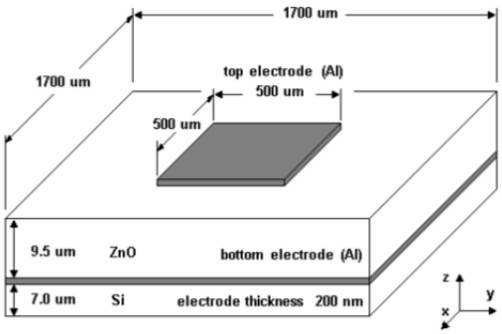

Figure 2. 3D suspended resonator structure.

In order to identify spurious modes, the mechanical displacement for four modes has been calculated, as displayed in Figure 3.

The first mode is the so-called thickness extensional mode. It corresponds to the maximum energy coupling and to minimum mechanical losses. This mode is the one taken into account in 1D analytical models.

The second mode is a cavity mode. In FEM, in order to keep the problem size finite, the physical domain needs to be truncated. This truncation introduces artificial boundaries where artificial boundary conditions are considered. Domain truncation causes reflection of the waves on clamped lateral sides. Then a standing wave may appear at certain frequencies. Those spurious modes are modeling errors and will be suppressed by mesh apodization.

Standing wave modes are harmonic thickness extensional modes due to acoustic wave reflection on top electrode edges. They appear as spurious modes in the electrical response. In order to use this electrical response for oscillator or filter applications, we need to suppress these modes. Different solutions can be considered.

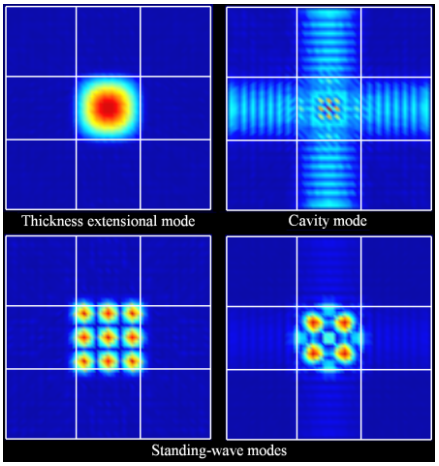

Figure 3. Top view of the suspended resonator mode shapes at resonant frequencies (The only top electroded region is the square in the middle).

2.2.3. Suppression of standing wave modes

2.2.3.1. Apodization

The first solution consists of cut a triangular part of the square top electrode and to paste it on another edge as shown in Figure 4. Then a quadrilateral electrode is obtained with no parallel sides [5].

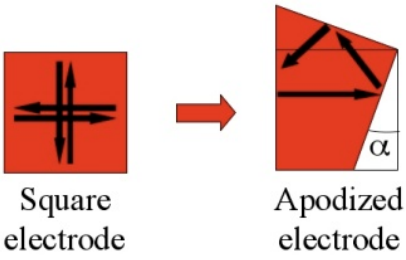

Figure 4. Apodization applied to a square electrode

Standing waves cannot appear since multiple reflections are not constructive. One can notice from Figure 5 that standing wave modes are not or weakly coupled as the apodization angle increases. A 3D simulation software enables the analysis of an entire apodized resonator and is very useful in this case for determining an optimum apodization angle.

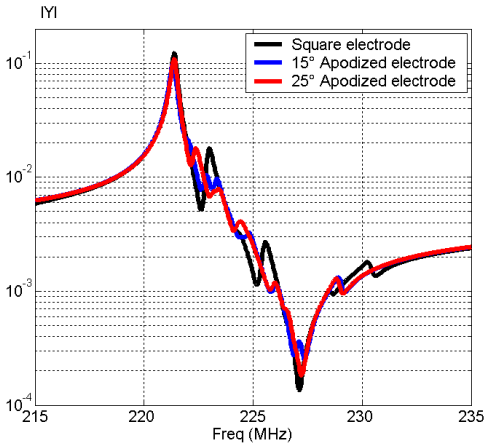

Figure 5. Apodized top electrode electrical admittance for two apodization angle values

2.2.3.2. Edge loading

Another solution proposed in [6] is considered. A narrow region is deposited at the edge of the suspended resonator top electrode as described in Figure 6. This thickened region constitutes a frame that matches the acoustic impedance and suppresses reflection on top electrode edges. Within certain optimum range for the edge region width, the resonator operates in a mode where the mechanical displacement is constant on the top electrode surface (Figure 7).

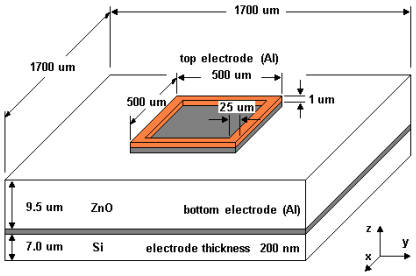

Figure 6. Framed top electrode suspended resonator 3D structure

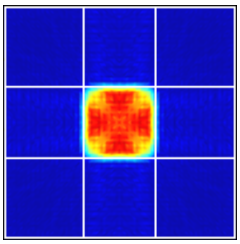

Figure 7. Framed top electrode suspended resonator thickness extensional mode

It can be observed, in Figure 8, that the electrical response is standing wave modes free. Standing waves on the top electrode are not coupled. Moreover, 3D resonant frequency tends toward 1D result.

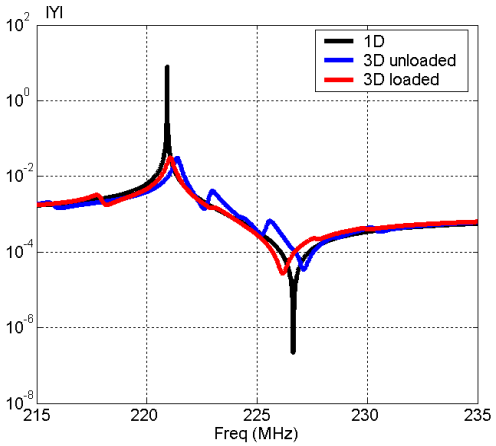

Figure 8. Framed top electrode suspended resonator admittance

2.2.3.3. Cavity modes suppression by resonator apodization

In order to identify spurious modes due to domain truncation, we have changed the distance from the top electrode edge to the structure edge (A=500 μm or 400 μm in Figure 9). We have found that resonant conditions and resonant frequencies for cavity modes change with cavity dimensions.

The mechanical displacement for those modes is displayed in Figure 9.

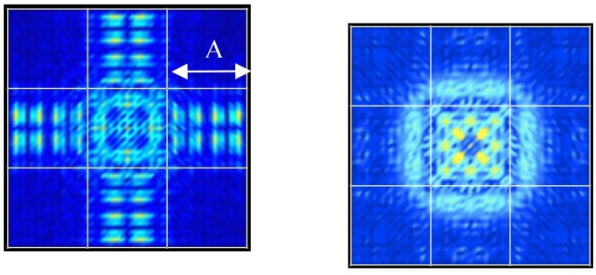

Figure 9. Mechanical displacement for two cavity modes (Top view)

While the mode which appears at *f = 224,5 MHz* is obviously a cavity mode, we can have doubts about the one at *f = 228,4 MHz*. In order to remove all doubts, we have applied the apodization technique to the resonator edges (Figure 10).

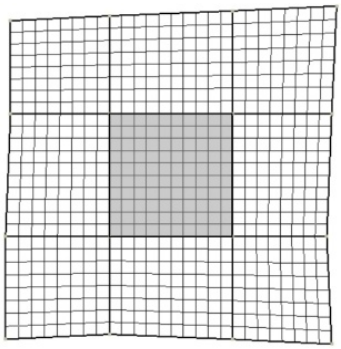

Figure 10. Apodized cavity (Top view) and mesh

We obtained an asymmetrical structure with no parallel sides. The irregular shape avoids phase reflections on the structure edges with constructive interferences, reducing the occurrence of standing waves.

One can observe in Figures 11, 12 and 13 that this technique enables to obtain an electric response free of spurious cavity modes.

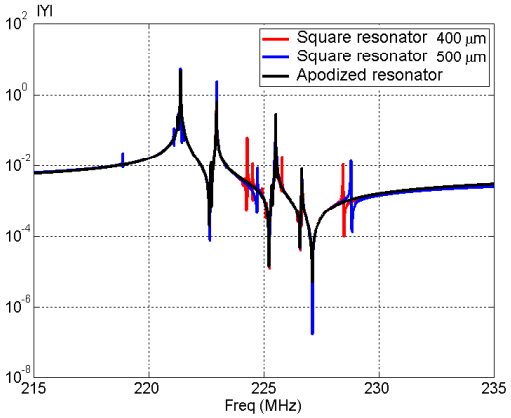

Figure 11. Suspended resonator electrical admittance

A full 3D FEM tool is very useful to analyze and to predict the behavior of complex structures. One can take into account non-homogenous structure and non-linear materials. Obviously it is the only method to compute 3D geometries. The shape of the mechanical displacement can be obtained to identify real or non-physical modes. Solutions have been proposed with apodized shape or with edge loading to remove parasitic modes.

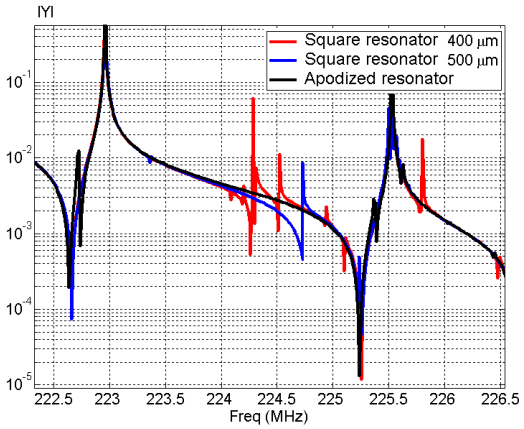

Figure 12. Suspended resonator electrical admittance around 224,5 MHz

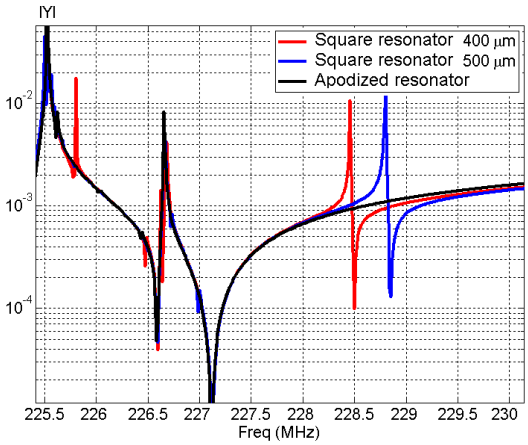

Figure 13. Suspended resonator electrical admittance around 228,4 MHz

3. Design of bulk acoustic wave filters

3.1. Implementation

The MBVD (Modified Butterworth Van Dyke) model, presented in Figure 14, can been used to compute the behavior of a BAW resonator [7]. Compared to the BVD model, the MBVD model incorporates resistances, which take into account losses in the piezoelectric material and in the electrodes.

This equivalent circuit resonates for two particular frequencies:

$$f_s = \frac{1}{2\pi\sqrt{Lm.Cm}} \tag{19}$$

$$f_p = f_s \sqrt{1 + \frac{Cm}{Co}} \tag{20}$$

fs and *fp* are known as the series and parallel resonant frequencies and correspond respectively to a minimum and to a maximum of the electrical impedance. *fs* and *fp* are related to the electromechanical coupling coefficient k_t^2 by:

$$k_t^2 = \frac{\pi^2}{4} \frac{f_p - f_s}{f_p} \tag{21}$$

Moreover, one can define Q_s and Q_p the quality factors of series and parallel resonances:

$$Q_s = \frac{2\pi f_s \, Lm}{Rm} \tag{22}$$

$$Q_p = \frac{1}{2\pi f_p \, Co \, Ro} \tag{23}$$

For dimensioning a BAW filter, each resonator is represented by its MBVD model and the synthesis of the BAW filter is carried out by optimizing each resonator with respect to a specified target.

BAW filters are usually implemented arranging series and shunt resonators. Basic resonator arrangements, namely ladder and lattice configurations, are defined as shown in Figures 15 and 16.

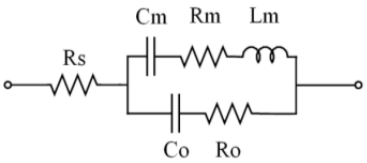

Figure 14. MBVD model of a BAW resonator

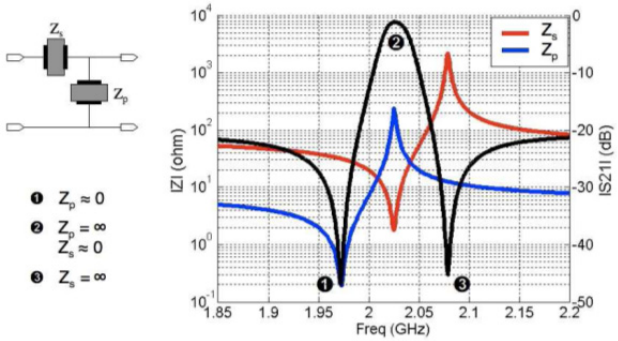

Figure 15. Electrical impedance of shunt and series resonators for providing a band-pass filter with a ladder network

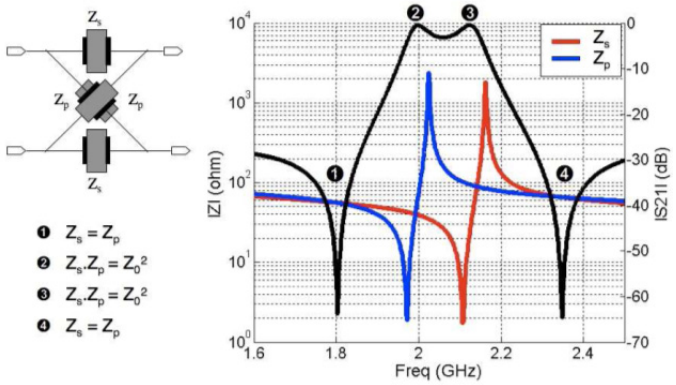

Figure 16. Electrical impedance of shunt and series resonators for providing a band-pass filter with a lattice network

The ladder configuration presents a high rejection close to the filter passband but a poor out of band rejection. On the other hand, the lattice filter exhibits higher out of band rejection but a poor rejection close to the filter passband. Combining these two configurations, one can obtain a mixed ladder-lattice filter with very good properties, as shown in Figure 17. S_{21} parameter is the forward transmission coefficient of the filter.

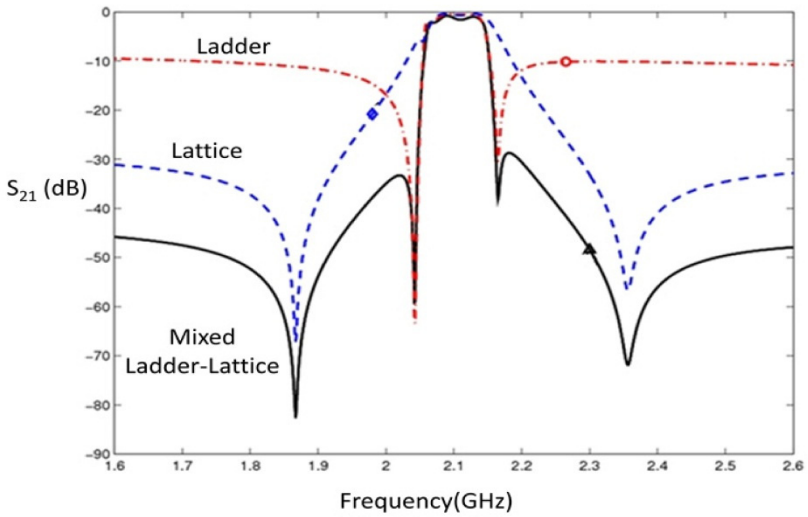

Figure 17. Behavior of the mixed ladder lattice filter.

3.2. Synthesis

Regarding the synthesis, each resonator is characterized by several fixed technological parameters obtained by electromechanical modeling or process characterization:

- k_t^2, the electromechanical coupling coefficient
- Q_s, the quality factor at series resonant frequency
- Q_p, the quality factor at parallel resonant frequency
- ε_r, the piezoelectric material permittivity
- $R_{[]}$, the square resistance of electrodes

The remaining variable parameters are:

- A, the surface of the top electrode ($A = L.W$ where L and W are the length and the width of the top electrode respectively, the aspect ratio L/W remaining generally the same for all electrodes)
- d and l: the thickness of the piezoelectric layer and the thickness of the loading layer respectively, which control the series resonant frequencies (f_s) of series and parallel resonators.

The lumped elements of the MBVD model are related to these parameters through the following expressions:

$$C_0 = e_0 e_r \frac{A}{d} \tag{24}$$

$$C_m = C_o \left[\left(\frac{f_s}{f_p} \right)^2 - 1 \right] \tag{25}$$

With

$$f_p = \frac{f_s}{1 - \frac{4}{\pi^2} k_t^2} \tag{26}$$

$$L_m = \frac{1}{C_m (2\pi fs)^2} \tag{27}$$

$$R_m = \frac{2\pi L_m fs}{Q_s} \tag{28}$$

$$R_o = \frac{1}{Q_p C_0 2\pi fp} \tag{29}$$

$$R_s = R_{[]} . \frac{L}{\omega} \tag{30}$$

One can note that Lm, Cm and Co can also be approximated directly by polynomial expressions of the layer thicknesses and resonator area as explained in section 2.1.3.

The thicknesses of the piezoelectric and loading layers and the area of each resonator are optimized with respect to the specifications. This optimization can be driven by the minimization of a cost function defined by the filtering pattern [8].

3.3. Electromagnetic co-simulation

The previous synthesis relies on MBVD models of BAW resonators, which do not take into account metallic losses or couplings due to interconnections and access ports. Since metallic lines used for connecting resonators have irregular geometries depending on the arrangement of resonators, models for such elements cannot be implemented in a synthesis tool. Nevertheless a simulation is possible a posteriori with the layout of the filter in order to estimate additional losses or to check eventual couplings due to metallic lines.

The layout of the filter to be realized can be drawn with an electromagnetic (EM) software, e.g. Momentum included in Agilent ADS [9]. Using such a EM software, all electrostatic and electromagnetic phenomena are characterized considering the geometry and the physical characteristics of stacked layers.

The electrostatic part of MBVD resonators (*Rs*, *Ro* and *Co*) is directly taken into account in the distributed model (related particularly to the area of resonators). However, the motional part (*Rm*, *Cm* and *Lm*) is modeled by lumped elements connected through internal ports as shown in the example given in Figure 18.

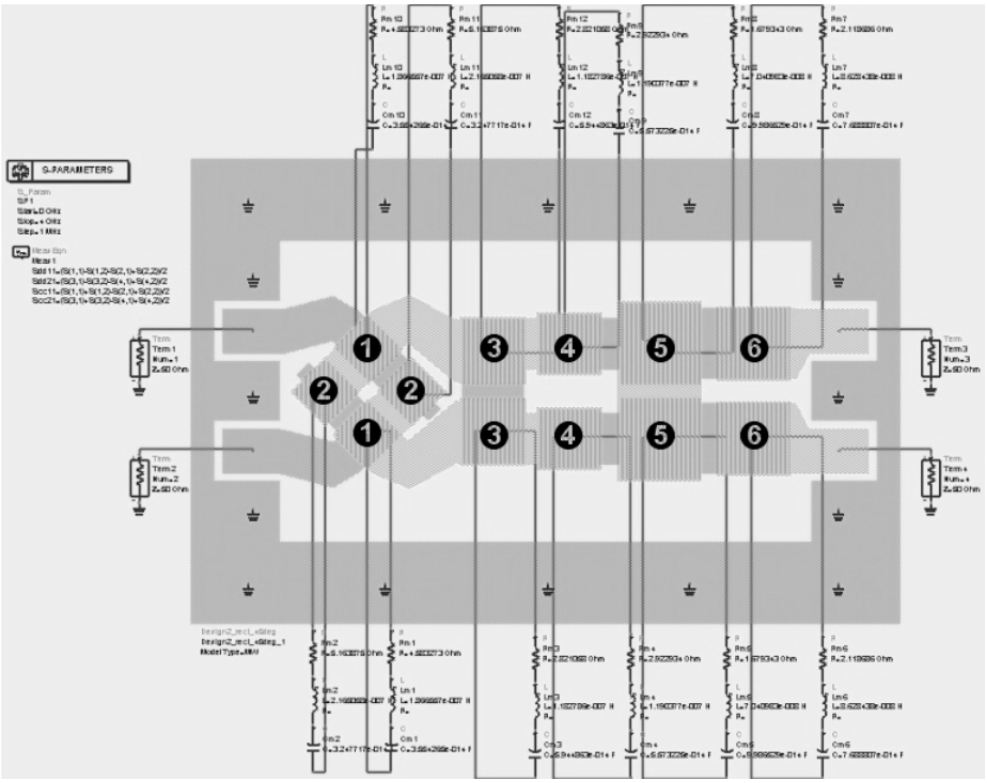

Figure 18. UMTS filter co-simulation

Figure 18 shows the co-simulation of a mixed ladder lattice filter in Agilent ADS/Momentum environment, including the layout and the motional parts directly derived from the previous synthesis.

4. Fabrication and characterization of BAW resonators and filters

4.1. Single resonator

Several BAW devices have been designed using the method proposed previously. Molybden is chosen as electrode material and the sputtering method is used. Therefore, AlN films have been deposited in (002) direction with the c-axis perpendicular to the substrate surface [10-13]. The optimized resonators and filters with the proposed method have been fabricated by CEA-Leti [14]. Figures 19 and 20 show a Solidly Mounted Resonator (SMR) resonator and a comparison between the simulated result and the measurement data respectively. The apodization of the top electrode was used to avoid parasite modes. One can observe a good agreement between simulations and measurements. S_{21} and S_{11} parameters are respectively the forward transmission and the reflection coefficients of the filter.

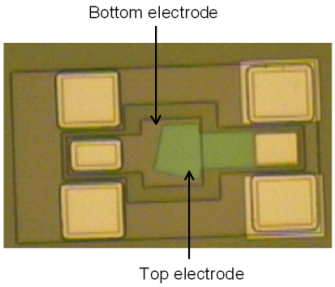

Figure 19. Structure of SMR resonator

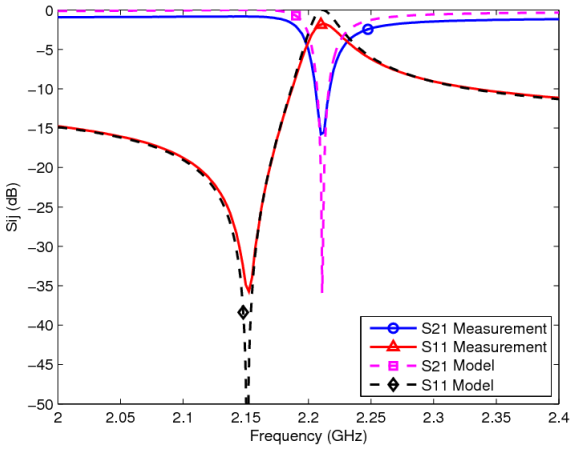

Figure 20. Comparison between the simulated result and the measurement data for SMR resonator

The resonant frequency is 2.212 GHz and anti-resonant frequency is 2.152 GHz, which leads to a coupling coefficient k_t^2 equal to 6.69%. The quality factor of this resonator is around 200.

4.2. 2-pole and 3-pole ladder filters

2-pole and 3-pole filters shown in Figure 21 were fabricated by CEA-Leti. Measurements and simulations for each filter are presented respectively in Figures 22 and 23. One can observe a good agreement between the measured responses and the simulated ones. The measured response of the 2-pole filter presents a passband of 55 MHz centered at 2.13 GHz (fractional bandwidth of 2.58 %) and the insertion losses are about 1.5 dB. Similarly, the 3-pole filter shows a 54 MHz passband at 2.13 GHz (FBW: 2.53 %) and insertion losses of approximately 2 dB.

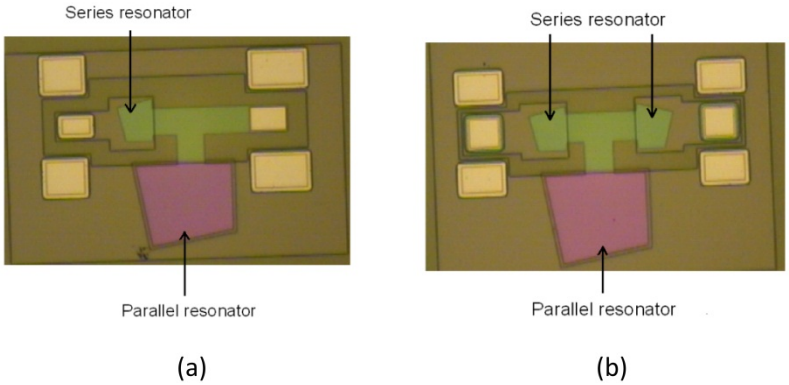

Figure 21. (a) Fabricated 2-pole filter. (b) Fabricated 3-pole filter (top view).

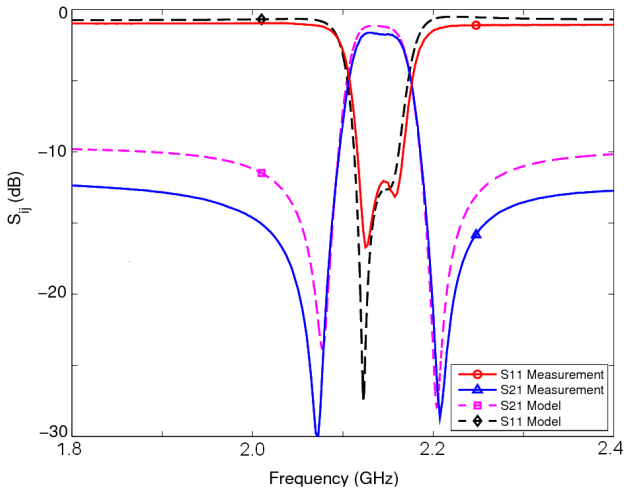

Figure 22. Measured and computed responses (model with losses) of the 2-pole filter

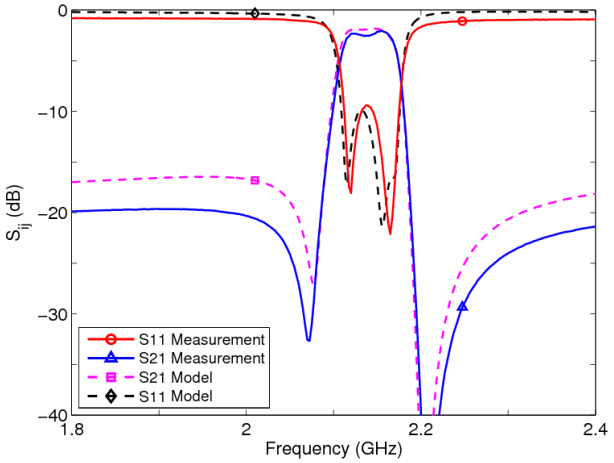

Figure 23. Measured and computed responses (model with losses) of the 3-pole filter

4.3. Differential ladder and lattice filters

Bandpass filters have been synthesised with differential structures (100Ω input/output impedance). These filters have been fabricated by CEA-LETI and UPM (Universidad Politécnica de Madrid) [15]. Each resonator is deposited on a Bragg mirror (SiN/SiOC) and is built with an Aluminium Nitride (AlN) piezoelectric layer and two Iridium (Ir) electrodes. With this technology, top electrode thickness is defined in order to act like a loading layer [16, 17] and to reach desired resonant frequency. Ir electrodes are utilized in order to enhance electromechanical coupling [18]. Iridium is a metal that presents a high-density [19] which leads to a high acoustic impedance, a low electric resistivity, and a specific crystal structure that promotes the growth of AlN films of excellent piezoelectric activity [20].

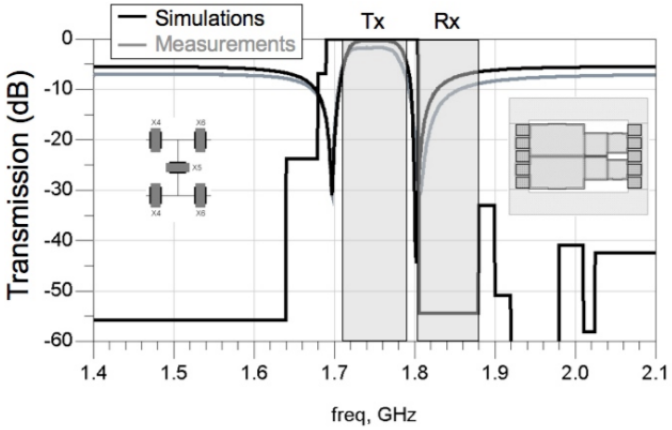

Figure 24. 1.5-stage ladder filter compared to UMTS standard

One can notice that there is a good agreement between simulated and measured responses in Figures 24 and 25. As electrical losses of Iridium were not characterized before simulation, they were not taken into account. Measured insertion losses are about 3dB for ladder structure and 6dB for lattice structure. A good out of band rejection is obtained, only limited by measurement noise.

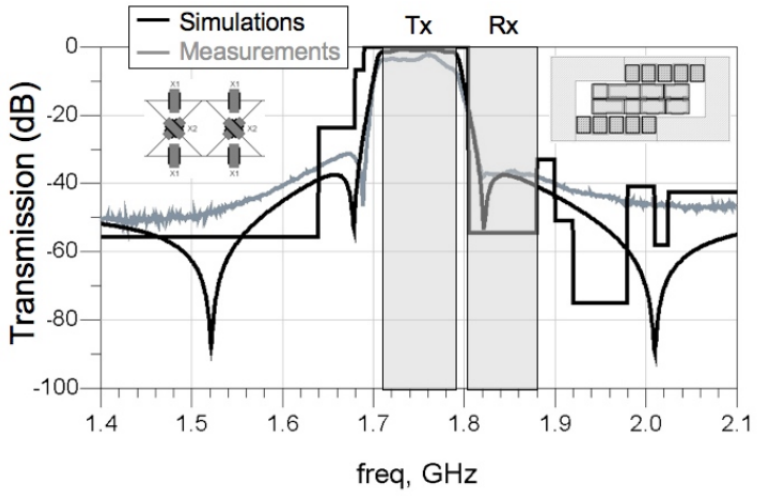

Figure 25. 2-stage lattice filter compared to UMTS standard

5. Integration of BAW components in a transmitter module

This section deals with the development of a BAW-SMR technology for application to mobile multi-standard communication terminals. UMTS and DCS1800 were chosen as targeted standards to validate a bi-standard BAW-based RF architecture, presenting both reconfigurability of active parts and integration of BAW technology.

This section presents the first demonstration of a complete UMTS transmitter including a CMOS 90nm digital RF signal generator connected to a BAW filter, a Power Amplifier (PA) stage and a BAW duplexer. Although the active part was originally designed for multi-mode purposes, UMTS standard was chosen to illustrate the proof of concept. The purpose is to emphasize the use of BAW-based structure for wireless mobile communications.

In the first section the proposed multi-standard transmission chain will be detailed, and a focus on the transmit BAW filter will be discussed. The design and measurement results of the stand-alone filter will then be presented before talking about the advantages of this filter with the RF signal generator. The BAW duplexer will be described and the measurement results of this filter will be detailed. Finally, the full transmitter test bench will be highlighted and the measurement results commented on.

5.1. RF signal generator

5.1.1. Third-order delta-sigma modulator

The architecture presented in Figure 26 is clearly aimed at future software defined terminals by pushing the band or standard specific components as close as possible to the antenna. The targeted standard is UMTS, one of the main mobile communication standards in Europe using 1920 – 1980 MHz frequency band for TX and 2110-2170 MHz frequency band for RX. The architecture could easily be extended to additional standards such as DCS or PCS at the cost of extra BAW filters for the appropriate frequency bands.

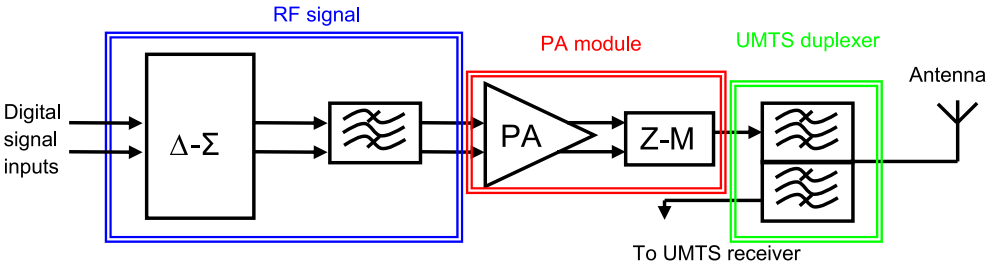

Figure 26. Modules definitions for first single standard UMTS transmitter

Two oversampled low-pass ΔΣ stages representing I and Q channels, work synchronously to generate a high sample rate 1-bit output stream [21] that feeds a digital image-reject mixer [22]. This latter stage produces a high frequency sampled two-level RF signal which exhibits very good in-band performances and a quantization noise shaping due to ΔΣ modulation [21]. A first stage of filtering precedes the power amplifier whose matching network converts a nominal single ended load impedance of 50 Ω to the optimal impedance for the active stage. A duplexer is inserted in order to isolate the receiver from the transmitter while enabling them to share a common antenna.

The UMTS transmit filter is designed on a ladder-lattice topology with 50 Ω differential input - 100 Ω differential output ports to benefit from advantages of both structures. This filter aims at meeting the standard emission mask by lowering the out-of-band quantization noise. Figure 27 shows the output spectrum of the digital RF signal generator and indeed justifies that the transmitter requires a large amount of out-of-band filtering at the output of the ΔΣ modulators. The most stringent specification for UMTS is the required rejection (50 dB) in the RX band (2110 MHz - 2170 MHz). It is very difficult to reach such a high rejection at a very close bandwidth from the center frequency band. A typical lattice BAW based filter exhibits a typical attenuation of roughly 40-45dB. Consequently, the insertion of a duplexer in the UMTS transmission chain is required to achieve this high attenuation in the RX band as well as its isolation between the TX and RX paths. The design and measurement results of these BAW-based structures are presented in the following sections.

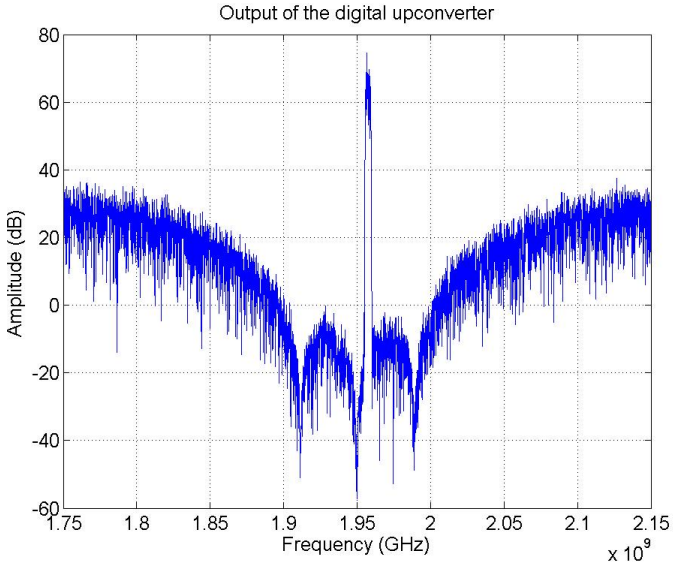

Figure 27. Spectrum of a ΔΣ modulated signal, up-converted around the RF carrier.

5.1.2. BAW filter

5.1.2.1. Filter synthesis

The synthesis of a UMTS filter has been performed [23], where a passband is needed for the 1920 – 1980 MHz range. Important constraints of the UMTS standard [24] are a high rejection and a high selectivity. To achieve these performances, a differential mixed ladder-lattice filter topology [25] with 100Ω differential impedance has been proposed. As explained in section 3, a mixed ladder-lattice filter as shown in Figure 28, provides sharp band edges and a good rejection in the stopband.

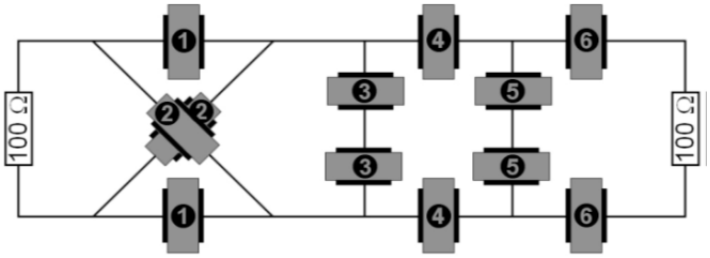

Figure 28. UMTS filter topology

After synthesis, optimal technological data for unloaded and loaded resonators are found as listed in Table 1. Related MBVD elements of each resonator are listed in Table 2 and the scattering parameters are given in Figure 29.

	fs (MHz)	*fp* (MHz)	K^2eff (%)	*Qs*	*Qp*
Unloaded	1954	2004	6.2	500	300
Loaded	1898	1946	6.1	500	300

Table 1. Unloaded and loaded resonators given technological data

		X1	X2	X3	X4	X5	X6
Elements values	*Rm* (Ω)	4.58	5.16	2.82	2.92	1.68	2.12
	Lm (nH)	186.6	216.5	118.3	119	70.4	86.3
	Cm (fF)	35	32	59	56	100	77
	R0 (Ω)	0.39	0.43	0.23	0.25	0.14	0.18
	Co (pF)	0.68	0.63	1.16	1.07	1.94	1.47
	Rs (Ω)	0.19	0.17	0.19	0.20	0.23	0.22

Table 2. MBVD elements values of optimised UMTS filter

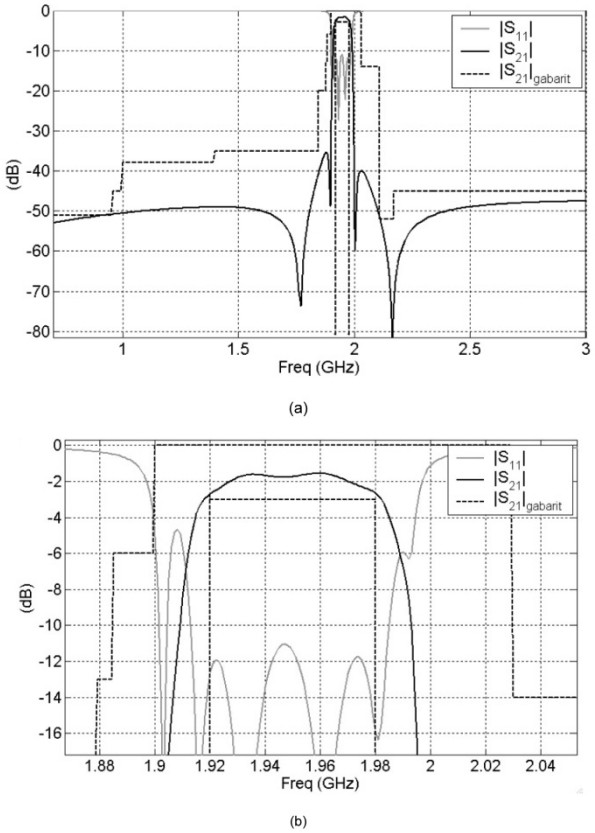

Figure 29. Scattering parameters of the UMTS filter: (a) wide band performance, (b) in band performance, compared to UMTS standard

One can observe, in Figure 30, that scattering parameters completely fulfill the specifications. Moreover, the layout of the filter has been co-simulated with a 2.5D electromagnetic software in order to estimate additional losses and to characterize eventual couplings due to metallic lines. As shown in Figure 30, the co-simulation is still in line with the specifications.

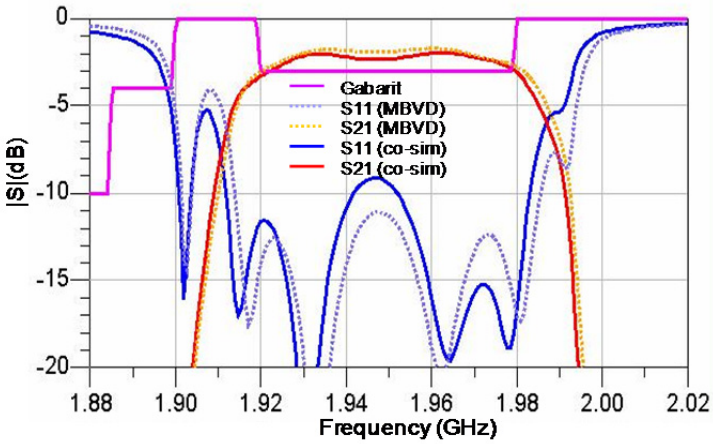

Figure 30. EM co-simulation of the UMTS filter, compared to UMTS standard

5.1.2.2. Fabrication and measurements

The filter has been fabricated by CEA-Leti. Each resonator is deposited on a Bragg mirror (SiN/SiOC), using an Aluminium Nitride (AlN) piezoelectric layer, two Molybdenum (Mo) electrodes and a Silicon Oxide (SiO2) loading layer. A photo of the filter is presented in Figure 31. The measured unpackaged quality factor at resonance frequency is close to 800 for the series resonators and close to 300 for the parallel ones. The measured response of the filter is presented in Figure 32. Insertion losses are around 3 dB and the required rejection and selectivity are fulfilled. The bandwidth is slightly reduced due to a lower resonant frequency for series resonators during fabrication

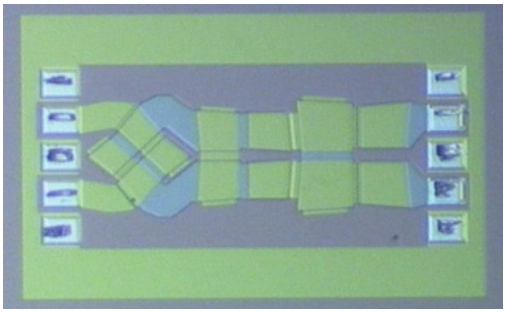

Figure 31. Fabricated filter with differential accesses.

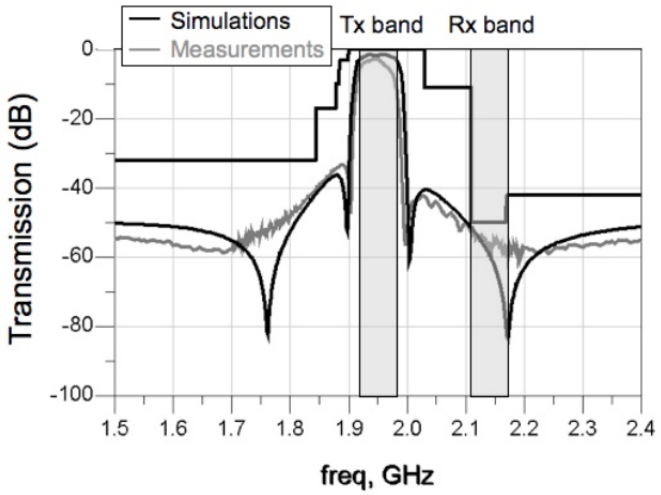

Figure 32. Measurement of the UMTS filter, compared to UMTS standard

5.2. Complete UMTS transmitter

5.2.1. RF Signal generator

The all digital RF signal generator architecture is presented in Figure 33. A first stage oversamples the baseband I and Q signals to reach the modulator frequency. The principle of ΔΣ modulation and digital mixing has been explained in section 5.1 and one can find further explanations in [21]. The generator output signal is a very high speed 1-bit signal with bandpass shaped quantization noise centered on the standard transmit band. The differential output buffer is able to drive a differential 50Ω load with a 1V power supply, at very low output impedance of 0.6Ω. As the BAW filter needs a 50Ω differential input impedance match, 25Ω resistors need to be inserted between the signal generator and the BAW filter. This very simple passive and unfortunately unmatched matching network degrades the filter transfer function, introducing ripple in the pass band and lowering out-of-band attenuation. Both the RF signal generator and the BAW filter are molded with a resist on a module which is then soldered on a larger PCB. The output of this subset circuit is 100 Ω differential [26].

The baseband input signals are generated by an external Arbitrary Waveform Generator (Tektronix AWG 420), in which a Matlab sequence has been programmed to generate a WCDMA modulated signal on I and Q channels. The external clock reference comes from a synthesizer delivering a clock signal at 2.6GHz with an output level of –5dBm. This clock is the nominal frequency clock of the modulators and of the digital image-reject mixer and fully determines the center frequency of the RF signal. Using a 2.6GHz, the ΔΣ generator outputs an RF modulated signal at 1.95GHz using the first image-band.

The measurement results (Figure 34) consist of a spectrum analysis of output signals to evaluate the benefits of using BAW filtering in a ΔΣ modulation approach. It clearly shows

that the out-of band quantization noise nearby the central bandwidth has been reduced below the noise level of the spectrum analyzer in this setup, due to the near-band high rejection of the ladder BAW filter configuration. Emission specifications in DCS are satisfied whereas more than 20dB of attenuation is still needed in UMTS RX band. Far-band filtering (thanks to lattice configuration) is also efficient, resulting in more than 35dB attenuation at low frequencies. In the first image band, the measured ACLR are 43 and 42dB, respectively at 5MHz and 10MHz offsets. The EVM is 3.7% and the measured channel power is -27dBm. This low value is due to the use of the first image and the loss in the series resistors.

The strongest constraint in UMTS transmission architecture is the very high level of rejection needed in the UMTS reception band which is very close to the transmission band. The measurement results show that a ladder-lattice BAW filter is not sufficient to fulfill this specification. A BAW-based duplexer, providing further isolation between both signal paths is consequently mandatory and will be described in the following section.

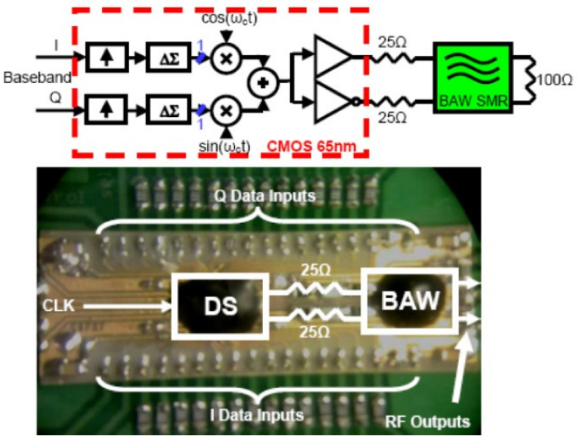

Figure 33. Signal generator and BAW filter architecture (left), photograph of the DS modulator and BAW assembly

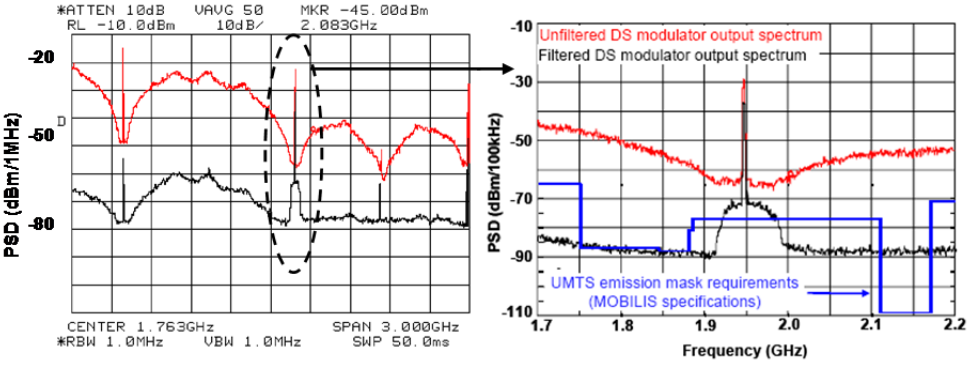

Figure 34. Delta-sigma digital generator output spectrum before (red) and after (black) BAW filtering

5.2.2. BAW duplexer

The BAW duplexer has been designed using a mix of the exposed BAW filter methodology and co-simulation with electromagnetic tools [27], [28], [29]. The topology of this duplexer is shown in Figure 35.

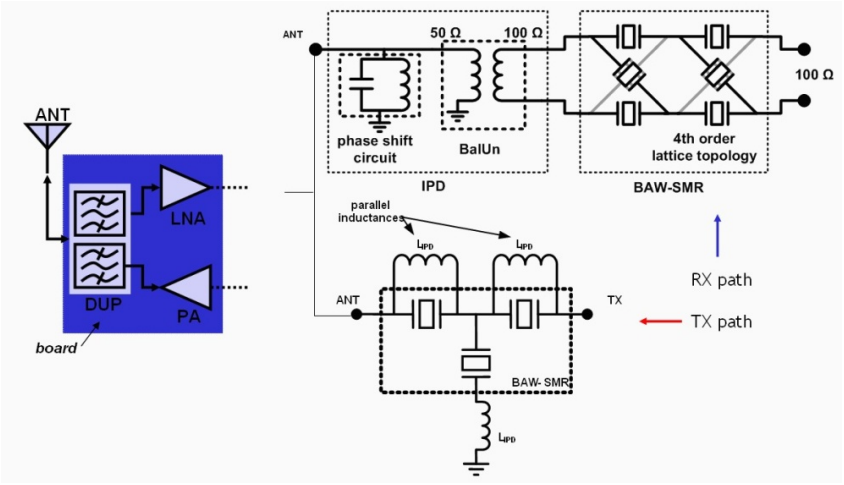

Figure 35. BAW duplexer topology

The BAW duplexer was made with two BAW filters and a glass substrate containing high quality passive elements (IPD from ST Microelectronics [30]). Each BAW filter occupies 1mm². The TX and RX filters were flip-chipped on the 3.9x3.9mm² substrate, as shown in Figure 36.

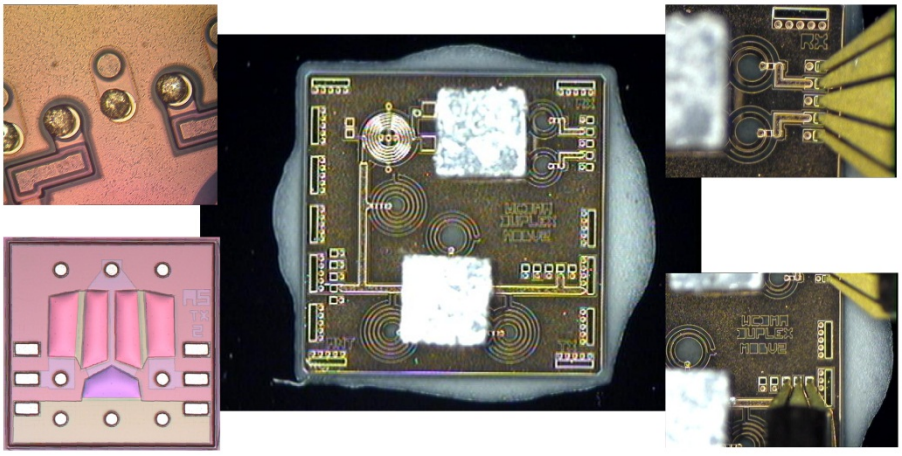

Figure 36. Left: Photograph of bumps and micropackaged TX filter. Center and right: On probe measurement of the BAW duplexer

The on-probe measurement of the duplexer is performed in two steps, for TX and RX paths respectively. This is due to calibration restrictions: two ports are 50 Ω single ended and the third one is a 100 Ω differential port, and on probe calibration of the vectorial analyzer is not guaranteed in these conditions. Figure 37 shows the comparison between probe measurement and backward simulation (taking into account of shifted components compared to expected elements in initial simulation). It shows globally a good fitting. The

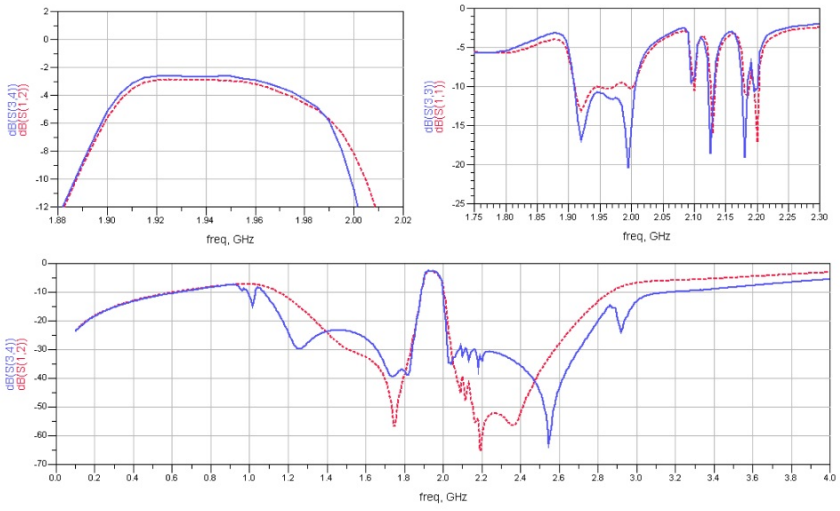

(a) BAW filter behavior (Tx path)

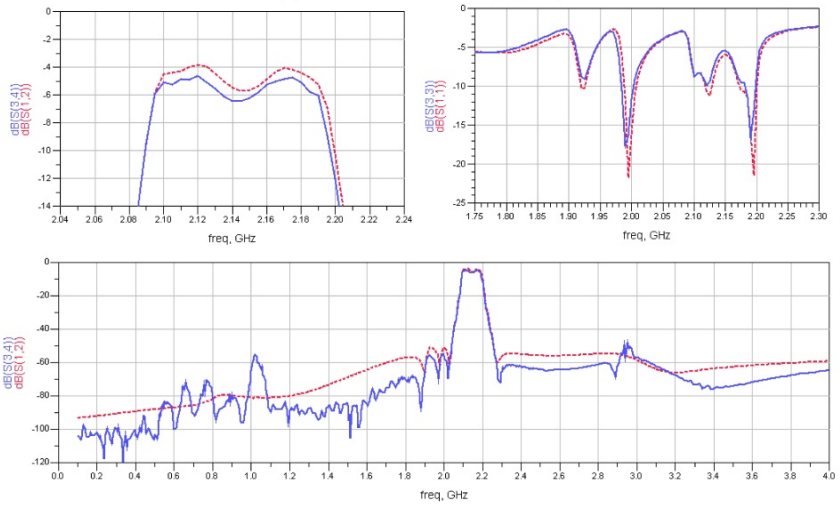

(b) BAW filter behavior (Rx path)

Figure 37. On probe measurement (blue) and simulation (BAW) – (a) TX path, (b): RX Path

only strong difference is the TX isolation at the RX frequency, which is due to grounding effects; it disappears when the ground is bounded. It should be noticed that because of the one-path measurement conditions, the other path is open, leading to a strong mismatch in the adjacent band. Moreover, the unexpected low coupling factor of the resonators and the especially balun variations explain the relatively low performances of this duplexer.

When mounted on board as shown in Figure 38, the BAW duplexer exhibits approximately the same performances as on probe, with a better out-of-band rejection. The RX rejection in the TX path is better than 40dB, the TX rejection in the RX path is better than 45dB, the TX insertion loss evolves from 2.6dB to 4.6dB in the upper border of the band, and the RX insertion loss falls from 4.5 to 6dB mainly due to the balun mismatch.

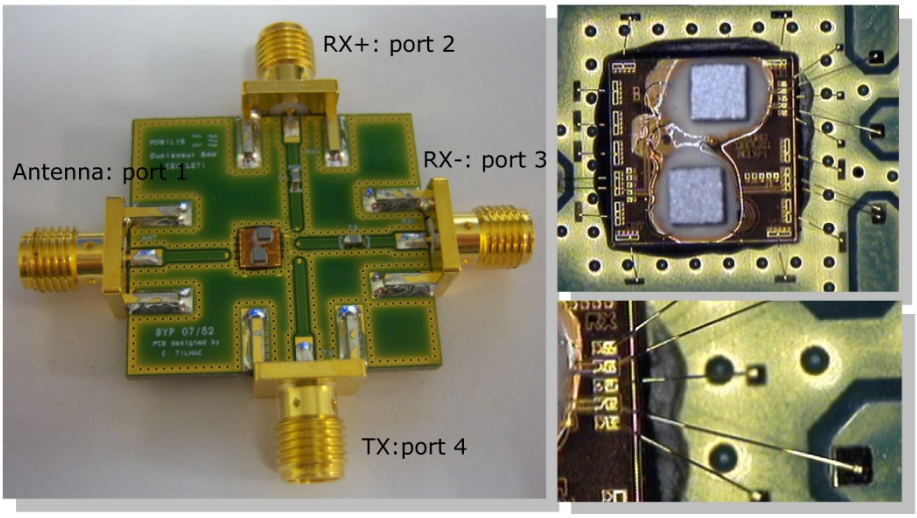

Figure 38. On board mounting of the BAW duplexer.

5.2.3. Complete transmitter test bench and measurement results.

Figures 39 and 40 present the measurement setup. Two test benches have been implemented: one with the RF signal generator feeding the transmit BAW filter and the PA module, and the second one is made of the latter test bench which has been completed by the BAW duplexer to get the complete transmitter.

At the differential output of the RF signal generator board, the BiCMOS7RF differential input – single ended output PA is connected. Isolators are placed on each signal path between the two boards. The PA exhibits a peak power gain of 13dB at 1.7GHz and almost 500MHz of -3dB bandwidth with an output compression point of 27.5dBm showing that this stage will not contribute to non-linearity with output power below 20dBm. The power gain at 1.95GHz is 10.3dB. Figure 41 presents the measured output spectrum for the signal at the output of the PA module.

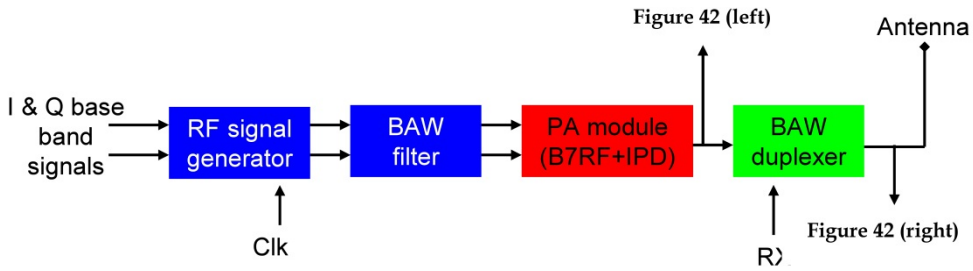

Figure 39. Test fixture for the full transmitter

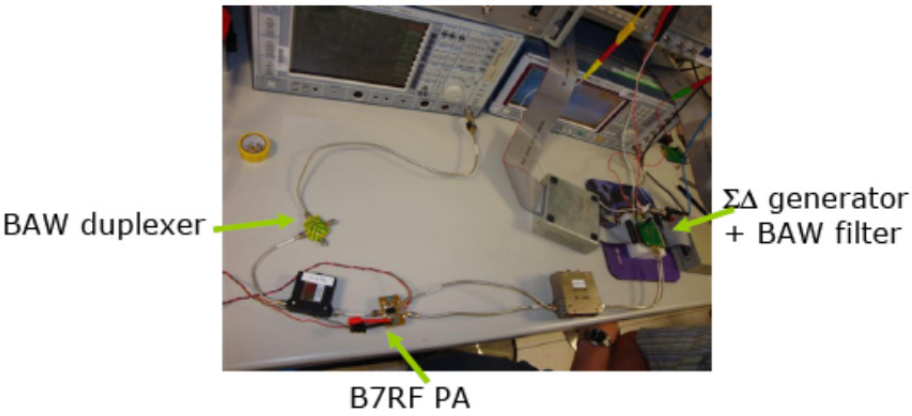

Figure 40. Measurement setup for filtered ΔΣ+ B7RF PA + BAW duplexer (full transmitter)

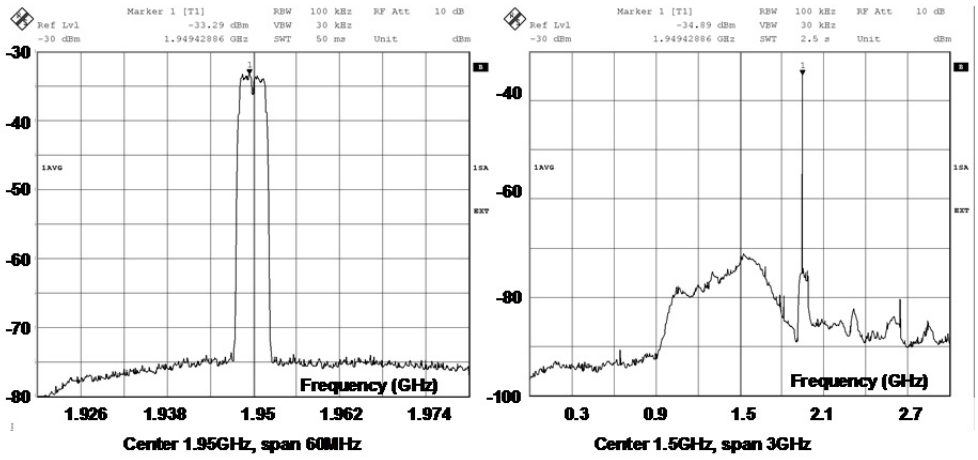

Figure 41. Output spectrum of the power gain stage, zoomed on the bandwidth (left) and full span (right)

One can observe that as the signal level at the input of the PA is low, there is no "visible" distortion on the signal (when looking in-band), and the ACLR level is preserved. When investigating a wider frequency window, we see the Sigma-Delta like lower side skirts re-growing in the band due to the wide-band amplification of the B7RF PA. Finally, a 42dB ACLR at 5 and 10MHz from the carrier for a -17.3dBm integrated power is obtained. EVM has been measured to be 4%.

At the single-ended output of the B7RF power amplifier, an isolator and the BAW duplexer are connected on the Tx input. The output chain measurements are done on the antenna pin of the duplexer demo-board, while the differential output toward the Rx path is shunted to 50 Ω loads. In figure 42, the filtering role of the duplexer Tx path on the overall transmitted signal is clearly shown. The ACLR constraints are generally preserved through the complete transmission chain. Moreover, the low-side spectrum re-growth observed in figure 42 is swept over by the BAW duplexer Tx filtering path. Finally, a 41dB and 41.7dB ACLR respectively at 5 and 10MHz from the carrier for a -20.8dBm integrated power is obtained. EVM has been measured to be 5%.

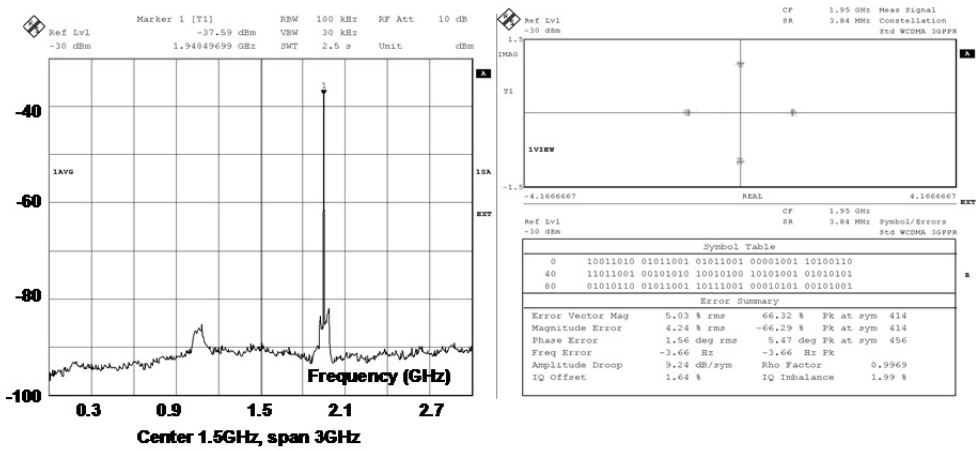

Figure 42. Measured wide-band output spectrum and EVM feature for the full transmitter (filtered ΔΣ + B7RF PA + BAW duplexer)

The complete transmitter is in line with the ACLR and EVM specifications. The transmitter was not able to fulfill the transmit power specifications due to some discrepancies on the distributed gain over the chain. Nevertheless, spurious emission requirements are almost fulfilled, thanks to the BAW high out-of-band rejection. The goal of the presented results was to demonstrate a novel type of Software Defined Radio transmitter architecture for W-CDMA (and DCS) standard(s) with BAW based filter and W-CDMA duplexer. Extra gain should be inserted into the whole transmission chain at the price of an increase in EVM and non-linearity degradation (lowering the ACLR).

6. Conclusion

In this chapter several methods for BAW devices simulation have been presented and investigated. Regarding the efficiency and the rapidity of the needed computation, designers could choose the 1D, the co-simulation piezoelectric equations and 2.5 D simulations or the full 3D Finite Element Method. The co-simulation equations and 2.5 D seems to be the best compromise between simulation time and quality of results. The detailed methods have been validated on several types of filters (Ladder, Lattice and mixed Ladder-Lattice). Optimization method and tools for filters have also been proposed to compute high quality filters (low insertion losses, high rejection, high pole number…).

BAW based filters and duplexers have then been presented and integrated in a complete UMTS transmitter highlighting the advantages of BAW devices.

Other piezoelectric materials are investigated and appear as promising solutions for realizing wide-band filters or sensors [31], [32].

Author details

Matthieu Chatras, Stéphane Bila, Sylvain Giraud, Lise Catherinot,
Ji Fan, Dominique Cros and Michel Aubourg
XLIM, UMR CNRS 7262, University of Limoges, Limoges, France

Axel Flament , Antoine Frappé , Bruno Stefanelli and Andreas Kaiser
IEMN, UMR CNRS 8520, Villeneuve d'Ascq, France

Andreia Cathelin
STMicroelectronics, TR&D, Crolles, France

Jean Baptiste David and Alexandre Reinhardt
CEA-LETI, Grenoble, France

Laurent Leyssenne and Eric Kerhervé
IMS, UMR CNRS 5818, Université de Bordeaux, Talence, France

7. References

[1] K.M.Lakin, G.R. Kline, K.T. Mccarron, "High Acoustic Resonators and Filters", 1993 IEEE Microwave Symp. Digest, 3, pp 1517-1520

[2] K. Y. Hashimoto, "RF Bulk Acoustic Wave Filters for Communications", Artech House, 2009.

[3] A. Shirakawa, JM. Pham, P. JarrY, E. Kerherve, "FBAR Filters Synthesis Method and Reconfiguration Trends", Chapter 3 of Microwave Filters and Amplifiers book, pp.19-47, Research Signpost, 2005.

[4] Lakin, K. M., Kline, G. R., and Mccarron, K. T., "Development of Miniature Filters for Wireless Application," *IEEE Transaction on Microwave Theory and Techniques*, Vol.43, 2933-2939, 1995

[5] K. M. Lakin and K. G. Lakin, « Numerical Analysis of Thin Film BAW Resonators », *Proceedings of Ultrasonics Symposium*, Vol. 1, pp. 74-79, October 2003.

[6] R. Thalhammer, R. Aigner, « Energy loss mechanisms in SMR–type BAW devices », *Microwave Symposium Digest*, 2005 IEEE MTT-S International 12-17 June 2005

[7] J. F. Rosenbaum "Bulk Acoustic Wave Theory and Devices", Boston: Artech House, 1988

[8] L. Catherinot, S. Giraud, M. Chatras, S. Bila, D. Cros, T. Baron, S. Ballandras, P. Monfraix, L. Estagerie "A general procedure for the desing of BAW filters", International Journal of RF and Microwave Computer-Aided Engineering, September 2011, Vol. 21, Issue 5, pp 458-465.

[9] http://www.home.agilent.com

[10] Lanz, R.; Muralt, P. "Solidly mounted BAW filters for 8 GHz based on AlN thin films", IEEE Symp. on ultrasonics, 2003, Vol. 1, pp. 178-181.

[11] C. Cibert, C. Champeau, M. Chatras, D. Cros and A. Catherinot « Pulsed laser deposition of aluminum nitride thin films for FBAR application » Applied Surface Science 253 (2007) pp. 8151-8154

[12] H.P.Loebl, M.Klee, C.Metzmacher, W.Brand, R.Milson And P.Lok "Piezoelectric Thin AlN Film for Bulk Acoustic Wave (BAW) Resonators" Materials Chemistry and Physics, Vol. 79, pp. 143-146, 2003

[13] Ylilammi, J.Ella, M.Partanen and J.Kaitila "Thin Film Bulk Acoustic Wave Filter" IEEE Transactions on Ultrasonics, Ferroelectrics, and Frequency Control, vol. 49, No. 4, pp. 535-539, April 2002

[14] http://www.leti.fr/en

[15] http://www.upm.es/internacional

[16] E. Iborra, M. Clement, J. Olivares, S. Gonzalez-Castilla, J. Sangrador, N. Rimmer, A. Rastogi, B. Ivira, and A. Reinhardt, "BAW resonators based on AlN with Ir electrodes for digital wireless transmissions." 2008 IEEE Ultrason. Symp. Proc., (2008) pp. 2189-2192.

[17] B. Ivira, P. Benech, R. Fillit, F. Ndagijimana, P. Ancey, and G. Parat, "Self-Heating Study of Bulk Acoustic Wave Resonators Under High RF Power" IEEE Trans. Ultrason. Ferr. Freq. Control, 55, (2008). pp. 139-147.

[18] A. Reinhardt, F. de Crécy, M. Aïd, S. Giraud, S. Bila, and E. Iborra, "Design of Computer Experiments: A powerful tool for the numerical design of BAW filters" 2008 IEEE Ultrason. Symp. Proc., (2008) pp. 2185-2188.

[19] A. Devos, E. Iborra, J. Olivares, M. Clement, A. Rastogi, and N. Rimmer, "Picosecond Ultrasonics as a Helpful Technique for Introducing a New Electrode Material in BAW Technology: The Iridium Case", 2007 IEEE Ultrason. Symp. Proc., (2007) pp. 1433-1436.

[20] J. Olivares, M. Clement, E. Iborra, S. González-Castilla, N. Rimmer, and A. Rastogi, "Assessment of Aluminum Nitride Films Sputtered on Iridium Electrodes ", Ultrasonics Symposium 2007, pp 1401-1404.

[21] A. Frappé, A. Flament, B. Stefanelli, A. Kaiser, A. Cathelin, "An all-digital RF signal generator using high-speed ΔΣ modulators", IEEE Journal of Solid-State Circuits, art. No. 15, Vol.44, Oct. 2009

[22] Vankka, J. Sommarek, J. Ketola, I. Teikari, M. Kosunen and K. Halonen, "A Digital Quadrature Modulator with on-chip D/A Converter," IEEE Journal of Solid-State Circuits, Vol. 38, No. 10, pp. 1635-1642, Oct. 2003.

[23] S. Giraud, S. Bila, M. Chatras, D. Cros, M. Aubourg, "Bulk acoustic wave filter synthesis and optimisation for UMTS application", EuMW 2009, Rome

[24] 3GPP UE Radio Transmission and Reception (FDD) TS 25.101. Available at http:\\www.3gpp.org\

[25] A. Shirakawa, P. Jarry, J.-M. Pham, E. Kerhervé, F. Dumont, J.-B. David, A. Cathelin, "Ladder-Lattice Bulk Acoustic Wave Filters: Concepts, Design, and Implementation", International Journal of RF and Microwave Computer-Aided Engineering, 5 June 2008, pp.476

[26] A. Flament, S. Giraud, S. Bila, M. Chatras, A. Frappe, B. Stefanelli, A. Kaiser, A. Cathelin, *"Complete BAW filtered CMOS 90nm digital RF signal generator"*, Joint IEEE North-East Workshop on Circuits and Systems and TAISA Conference, 2009

[27] E. Kerhervé, J.B. David, A. Shirakawa, M. El Hassan, K. Baraka, P. Vincent, A. Cathelin, "SMR-BAW duplexer for W-CDMA application", Journal of Analog Integrated Circuits and Signal Processing,2010.

[28] A. Shirakawa, P. Jarry, J.M. Pham, E. Kerherve, F. Dumont, J.B. David, A. Cathelin, "Ladder-Lattice BAW Filters: Concepts, Design and Implementation" , International Journal of RF & Microwave Computer Aided Engineering (RFMiCAE), 2008

[29] P.Bradly, R.Ruby, J.Larsoniii, Y.Oshmyansky and D. Figueredo "A Film Bulk Acoustic Resonator (FBAR) Duplexer for USPCS Handset Applications" IEEE International Microwave Symposium Digest 2001, Vol.1, P367-370

[30] Calvez, C.; Person, C.; Coupez, J.; Gallée, F.; Gianesello, F.; Gloria, D.; Belot, D.; Ezzeddine, H. "Packaged hybrid Si-IPD anrenna for 60 GHz applications", EuMW 2010, pp683-686.

[31] M. Chatras, L. Catherinot, S. Bila, D. Cros, S. Ballandras, T. Baron, P. Monfraix, L. Estagerie "Large Band Pass BAW Filter for Space Applications"IEEE, IFCS, San Francisco, May 2011

[32] T. Baron, J. Masson, D. Gachon, J.P. Romand, S. ALzuaga, L. Catherinot, M. Chatras, S. Ballandras. "A Pressure Sensor based on HBAR micromachined structure" IEEE IFCS, New Port(USA), june 2010.